Refining Contribution at Hotspot and Emulsion Zones of Argon Oxygen Decarburization: Fundamental Analysis Based upon the FactSage-Macro Program Approach

PRASENJIT SINGHA

Examining the kinetics involved in the Argon Oxygen Decarburization (AOD) process, especially in the hotspot and emulsion zones within distinct reactors, can offer a deeper understanding of the refining mechanism in stainless-steelmaking. A predictive dynamic model has been formulated to estimate the effects of different refining processes, encompassing decarburization, desiliconization, demanganization, and chromium removal. The model includes a sub-model for heat loss calculation. The FactSage™ software, along with its macro programming capability, was utilized to incorporate thermochemical and kinetic information into the model. The model forecasts that the predominant chromium removal occurs within the hotspot zone, while carbon, silicon, and manganese removals occur in both the hotspot and emulsion zones. The predictions regarding the transient compositions of steel and slag, as well as the temperature of the steel bath, align with the plant data (Average of five heats), showcasing consistency.

I. INTRODUCTION

THE Argon–Oxygen Decarburization (AOD) process, a predominant method in global secondary steel production, accounts for over 75 pct of stainless-steel output.[1] Employing gas injection to enhance the refinement of liquid steel via rapid mixing, the AOD process is a dominant converter process that accelerates the chemical reaction process.[2] The refining process is intricate, involving the dynamic interplay of atoms, ions, and molecules at the interfaces of slag-metal, gas–metal, and slag–gas at elevated temperatures. This occurs concurrently with heat and mass transfer, and the process heavily relies on the cognitive abilities and expertise of the operator. Enhancing the refining process necessitates a profound understanding of the refining phenomena in the metal bath, hotspot, and emulsion zones. However, accurately determining the essential system parameters through experimentation is formidable.

Performing comprehensive numerical modeling of the entire AOD converter demands a significant allocation of computational resources. Consequently, mathematical modeling has emerged as the preferred approach to grasp the system's intricate nature and optimize operating parameters. In their research on the Argon–Oxygen Decarburization Converter, Chanouian et al.[3] examined the decarburization reactions occurring within a single gas bubble. The findings reveal that, under low-pressure conditions, a 60 mm oxygen gas bubble undergoes a rapid reaction with the melt and becomes saturated with carbon within a time span of 0.2–0.25 seconds. In their work, Ohno and Nishida[4] introduced a novel concept for decarburization within the AOD process based on bubble dynamics. Their proposal focused on the initial oxidation of chromium by injected oxygen, mainly taking place within a specific zone. Subsequently, chromium oxide generated in this process served as the oxidizing agent for carbon, which rises within argon bubbles. Asai and Szekely[5,6] introduced a mathematical model that characterizes the temperature and composition trajectories during the refining process. Visuri et al.[7,8] developed a novel reaction model to account for the reduction of top slag in the reduction stage by considering the thermodynamic equilibrium alongside a set of conservation equations for mass and heat at each time step. Recently, Visuri et al. also[9] investigated synthetic flux and fluorspar's effect in lowering

PRASENJIT SINGHA is with the Department of Metallurgical and Materials Engineering, Indian Institute of Technology Madras, Chennai, Tamil Nadu, India. Contact e-mail: psinghanifft@gmail.com

the melting point and viscosity of the slag. Kang et al.[10] demonstrated that chromium oxide is crucial in decarburization within low-carbon content zones. Ashok et al.[11] depicted that the efficiency of carbon removal in the Argon Oxygen Decarburization (AOD) process can be assessed through an empirical formula. It was observed that the carbon removal efficiency (CRE) shows an upward trend as the amount of carbon removed increases; however, it was noted that the efficiency did not surpass the 65 pct mark. Fruehan[12] created a reaction model to forecast carbon and chromium oxidation rates in the AOD stainless-steel-making process. The presence of Cr_2O_3 is of utmost importance in the oxidation of carbon, especially as it rises through the molten bath along with argon bubbles. In their study, Miyamoto et al.[13] discovered that altering the characteristics of slag, such as reducing its basicity or introducing elements like Al_2O_3 or CaF_2, had a beneficial impact on enhancing the rate of Cr_2O_3 reduction by carbon. This improvement was attributed to an increased proportion of the liquid phase within the slag. Conversely, Yokoyama and associates[14] observed a decrease in the reduction rate as the content of Al_2O_3 and MgO in the slag increased during the reduction stage. Nakasuga and their team[15–17] reported that adding fluxes like Al_2O_3 and SiO_2 to the slag facilitated the formation of early-stage liquid slag and improved chromium recovery rates. Furthermore, other researchers[18,19] provided insights into the refining characteristics of the AOD process. Jarvinen et al.[21] elaborated on the process of decarburization and slag formation occurring in the AOD process during the decarburization stage. Wei and Zhu[22,23] presented a groundbreaking method to tackle oxidation–reduction reactions occurring at the interfaces between liquid steel and gas bubbles. Several other scientists have suggested[24–29] that multiple oxidation–reduction reactions occur simultaneously at the interface between liquid and gas bubbles. Nakasuga et al.[15,16] investigated the recovery rate of chromium from stainless-steel slag by applying a kinetic reduction model initially put forth by Shibata et al.[30]. Their research findings indicated that the reduction rate of Cr_2O_3 rises as the temperature increases. Furthermore, Gornerup and Lahiri[31] reported that higher temperatures decreased the incubation time and boosted the reduction rate of Cr_2O_3. Deo and Kumar's[32] reordered sequence outlines the logical flow of steps for predicting the weight percentages of C, Cr, Mn, and Si. Riipi et al.[33] also forecast the final compositions of Cr, C, Si, and Mn, as well as the slag compositions, by leveraging a methodology involving mass transfer and thermodynamic calculations. The computational methods have been employed to analyze the phase composition of AOD slags under operational temperatures in previous studies.[34–37]

Wimmer et al.[38] illustrated a higher bath diameter-to-height ratio and lower partial pressure of CO enhanced mass transfer rate inside the converter. Odenthal et al.[39] and Wupperman et al.[40,41] developed mathematical models to predict the stirring effect in an AOD process.

Wei et al.[42] reported pctC and pctCr in the bath as well as slag composition in slag and bath temperature as a function of blowing time. Illiander et al.[43] demonstrated bubble characteristics and fluid-slag dispersion behavior for different gas flow rates. Samuelsson et al.[44] developed a water-based model and determined the concentration of dissolved CO_2 in the water bath for different converters' geometries and tuyere numbers. Patra[45] calculated bath composition, temperature, practical use of argon gas, and critical control over final nitrogen content in stainless-steel. Ternstedt et al.[46] studied the effect of top slag on the gas penetration depth, fluid flow, and slag behavior under different nozzle diameters, nozzle numbers, and gas flow rates. They reported that the gas penetration depth generally increases linearly with an increased gas flow rate and a decreased nozzle size. The slag thickness increases linearly with an increased gas flow rate. Heikkinen et al.[47] figured out wt pct slag constitutes at different refining stages using FactSage. Rafiei et al.[48] reported wt pct losses of carbon and manganese depending on the initial concentration of species and temperature.
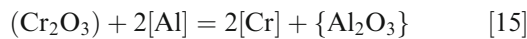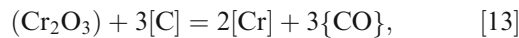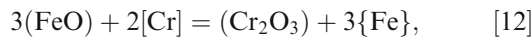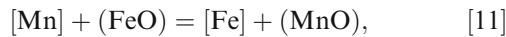
Recently developed a process module that accounts for thermodynamic and kinetic reactions based on the effective equilibrium approach (EERZ) concept using Thermo-Calc.[49,50]

The survival process models for the steelmaking converter excel in accurately predicting AOD process parameters like temperature, oxygen-blowing duration, and the chemical compositions of slag and steel. Nevertheless, the challenge lies in determining the transient compositions of liquid steel and slag, a task influenced by multiple reactors, free energy minimization, and various kinetic reactions occurring in the impact and emulsion zones.

The goal of this study is to gain a better understanding of how specific refining rates for elements like C, Si, Mn, and Cr removals are influenced by distinct emulsion and impact zones in the context of an operational AOD (Argon Oxygen Decarburization) process. This approach is expected to offer theoretical insights into the refining process during Argon Oxygen Decarburization, and it aims to introduce a practical tool that can be applied within the plant for implementation.

II. THERMODYNAMICS OF STAINLESS-STEEL PRODUCTION

The model formation considered the following important chemical reactions.

$$\{O_2\} = 2[O], \qquad [1]$$

$$[C] + [O] = \{CO\}, \qquad [2]$$

$$2[Cr] + 3[O] = (Cr_2O_3), \qquad [3]$$

$$[Si] + 2[O] = (SiO_2), \qquad [4]$$

$$[Mn] + [O] = (MnO) \qquad [5]$$

$$[Fe] + [O] = (FeO), \qquad [6]$$

$$\{CO\} + (FeO) = [Fe] + \{CO_2\}, \qquad [7]$$

$$[C] + (FeO) = \{CO\} + [Fe], \qquad [8]$$

$$[Si] + 2(FeO) = (SiO_2) + 2[Fe], \qquad [9]$$

$$[Si] + 2(MnO) = (SiO_2) + 2[Mn] \qquad [10]$$

$$[Mn] + (FeO) = [Fe] + (MnO), \qquad [11]$$

$$3(FeO) + 2[Cr] = (Cr_2O_3) + 3\{Fe\}, \qquad [12]$$

$$(Cr_2O_3) + 3[C] = 2[Cr] + 3\{CO\}, \qquad [13]$$

$$2(Cr_2O_3) + 3[Si] = 6[Cr] + 3\{SiO_2\}, \qquad [14]$$

$$(Cr_2O_3) + 2[Al] = 2[Cr] + \{Al_2O_3\} \qquad [15]$$
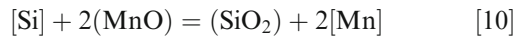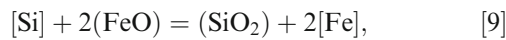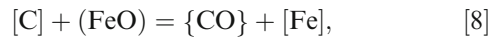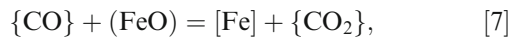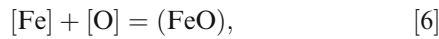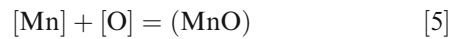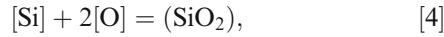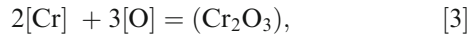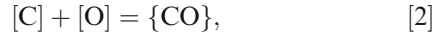
Equation [1]: Molecular oxygen (O_2) can be represented as two oxygen atoms [O]. Equation [2]: Carbon [C] reacts with oxygen [O] to form carbon monoxide (CO). Equation [3]: Two chromium atoms [Cr] react with three oxygen atoms [O] to produce chromium oxide (Cr_2O_3). Similarly Eqs. [4], [5], and [6], one Silicon [Si], manganese [Mn], and iron [Fe] react with oxygen [O] to form silicon oxide (SiO_2), manganese oxide (MnO) and iron oxide (FeO), respectively. This reaction Eqs. [1] through [6] typically occurs at the hotspot zone in the AOD converter. Equation [7]: Carbon monoxide (CO) reacts with iron oxide (FeO) to produce iron

[Fe] and carbon dioxide (CO_2). Equation [8]: Carbon [C] reacts with iron oxide (FeO) to form carbon monoxide (CO) and iron [Fe]. Equation [9]: Silicon [Si] reacts with two iron oxide molecules to produce silicon dioxide (SiO_2) and two iron atoms [Fe]. Equation [10]: Silicon [Si] reacts with two manganese oxide molecules to produce silicon dioxide (SiO_2) and two manganese atoms [Mn]. Equation [11]: Manganese [Mn] reacts with iron oxide (FeO) to produce iron [Fe] and manganese oxide (MnO). Equation [12]: Three iron oxide molecules react with two chromium atoms [Cr] to produce chromium oxide (Cr_2O_3) and three iron atoms Fe. Equation [13]: Chromium oxide (Cr_2O_3)) reacts with three carbon atoms[C] to produce two chromium atoms [Cr] and three carbon monoxide molecules (CO). Equation [14]: Two chromium oxide molecules (Cr_2O_3) react with three silicon atoms [Si] to produce six chromium atoms [Cr] and three silicon dioxide molecules (SiO_2) Eq. [15]: Chromium oxide (Cr_2O_3) reacts with two aluminium atoms [Al] to produce two chromium atoms [Cr] and aluminium oxide (Al_2O_3). The chemical reaction Eqs. [7] through [13] typically occurs at the emulsion zone in the AOD converter. The chemical reactions Eqs. [14] and [15] occur in the hotspot and emulsion zone during the reduction period.

A. Thermodynamic Database

In the current investigation on stainless-steel production, thermodynamic software FactSage$^{TM[51]}$ version 7.3 is used in conjunction with its macro capabilities. FToxid, FSstel, and FactPS databases of the FactSage system were considered for calculations. The phases considered during the calculations are given below:

Slag   The components of FToxide-SLAGA for the current calculation are Cr_2O_3-CrO- MnO-SiO_2–CaO–MgO–Al_2O_3–FeO–Fe_2O_3. Under reducing conditions, a slag phase Comprising Cr_2O_3–MnO–MgO–SiO_2–Al_2O_3–CaO–FeO, along with minor quantities of CrO and Fe_2O_3.

Hot metal The components in FSstel-Liqu for the current calculation are Fe–Cr–C–Si–Mn–Mg–Al–O.

Gases   The components in FactPS-GAS for the current calculation are C–O.

B. Model and Process Description

The structural configuration of the top-blown AOD converter, represented in Figure 1, consists of distinct regions that are conceptually treated separately. These distinct regions encompass metal bulk (reactor 1), slag bulk (reactor 2), hotspot (reactor 3), and emulsion (reactor 4) zones, and each undergoes specific treatment. The lower section of the converter is denoted as a metal bath (reactor 1), where the dissolution of scrap and ferroalloys (FeSi and SiMn) occurs. Conversely, the upper part corresponds to a slag bath (reactor 2), facilitating concurrent heat and mass transfer to dissolve
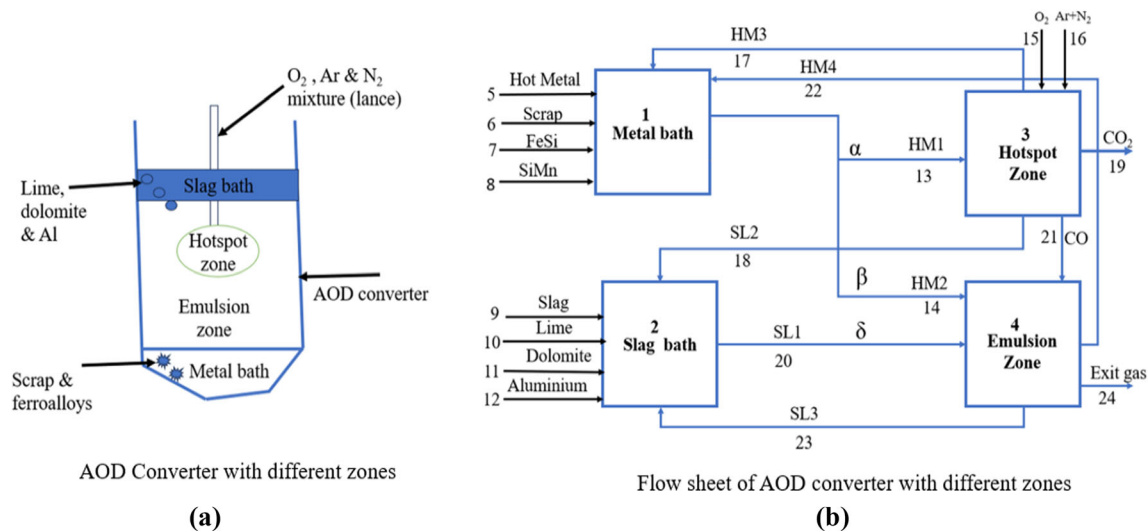
Fig. 1—AOD converter (*a*), and flow sheet of AOD converter with different zones (*b*).

lime, dolomite, and aluminum. The hotspot zone or reactor 3 is a crucial location where high-velocity oxygen, argon, and nitrogen jets impact the metal bath from the lance. Oxidation–reduction processes involving carbon, silicon, manganese, and chromium occur in this area. The unutilized section of the converter was designated as an emulsion zone or reactor 4, and the refining of the same elements as in reactor 3. After the reaction, the metal and slag phases from the reaction zone (reactors 3 and 4) were returned to their respective bulk phases (reactors 1 and 2), sustaining the refining process. In this model, the metal, slag, and gas phases were transported separately as streams (streams 5–24). The flowchart of the present work is shown in Figure 2.

This system introduces a mixture of hot metal, scraps, and ferroalloys into a metal bath through streams 5, 6, 7, and 8, respectively. Simultaneously, slag (stream 9), lime (stream 10), dolomite (stream 11), and aluminium (stream 12) are introduced into the slag bath. Oxygen and argon + nitrogen jets (streams 15 & 16) at supersonic velocity are directed into the converter (reactor 3) from the top side of the furnace, where oxygen dissolves in the liquid steel, promoting the oxidation of elements like carbon (C), silicon (Si), manganese (Mn), and chromium (Cr). A circulation stream is extracted from the metal bath (stream 13) and reintroduced at various stages within the hotspot zone to ensure a continuous process, supplementing the fresh metal input. The resulting liquid metal (stream 17, HM3) and liquid slag (stream 18, SL2) are continuously recirculated into the metal and slag bulk baths, respectively. Carbon dioxide (stream 19, CO_2) gas, generated within the hotspot zone, is released into the atmosphere. In the emulsion zone, streams 14 and 20 (HM2 and SL1), originating from the metal and slag bulk baths, are systematically introduced at each step. The liquid metal (stream 22, HM4) and liquid slag (stream 23, SL3)

are recirculated to their bulk baths (reactors 1 and 2). Carbon monoxide (stream 21, CO) gas, produced in the high-temperature zone (reactor 3), is used as a reducing agent upon entering the emulsion zone. The resulting gases (stream 24) exit the system as top gas.

C. Kinetic Consideration

The mass transfer coefficients in an Argon–Oxygen Decarburization (AOD) process converter are affected by the mixing energy rate introduced into the system through the top oxygen, argon supply, decarburization rate, and chromium removal rate. The mixing energy is imparted to the system by 4 components, first due to the impact of top-blown oxygen and argon supply by lance, and second due to rising carbon monoxide gas bubbles and chromium oxide droplets forming at different bath depths. The reaction phase fraction at each time step depends on the mixing energy or total energy imparted by various mechanisms as discussed above. This comprehensive energy originates from the oxygen and argon sources introduced at the furnace's top $\left(E_{O_2}^0 \text{ and } E_{Ar)}^0 \right)$ and the rates at which carbon and chromium are removed from the hot metal $\left(E_{decarb}^0 \text{ and } E_{chromiumremoval}^0 \right)$. Therefore, the equations[24–26] depict the variation in the fractions of metal (α and β) and the fraction of slag (δ) as a function of the total input energy (E_{total}^0) to the system, which imparts mixing, resulting in circulation streams across the reactors. The following equations Eqs. [16], [17], [19], [20] were used to calculate the total input energy or mixing energy into the system (E_{total}^0).

Metal is divided into two streams, denoted as stream 13 (α) and stream 14 (β), representing the fractions migrating toward the hotspot (reactor 3) and the emulsion zones (reactor 4), respectively. Additionally,
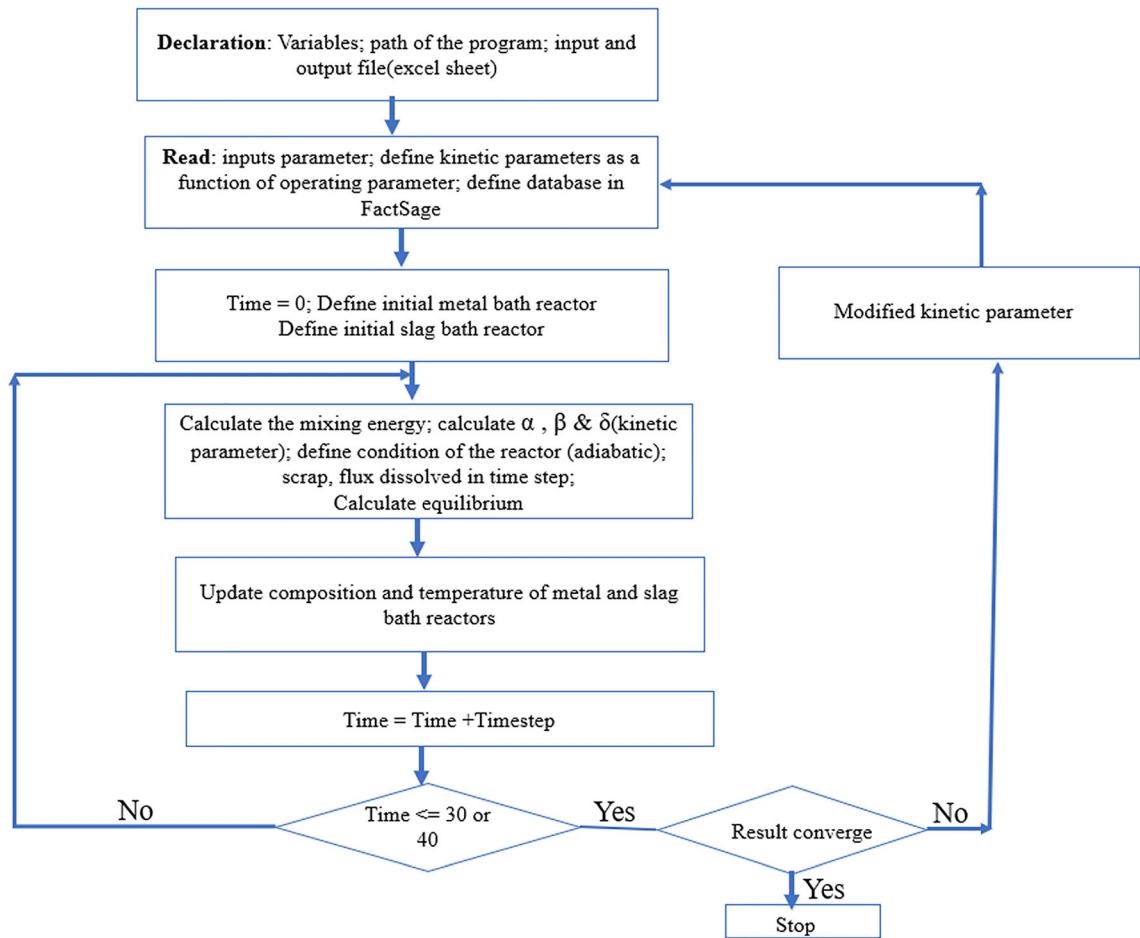
Figu. 2—flowchart of the present work.

δ signifies the proportion of slag entering the emulsion zone (reactor 4). These fractions, α, and β, along with δ, serve as mass transfer coefficients for hot metal or slag. It is essential to note that the composition and temperature of both α and β remain constant while the flow rates differ. In this context, the values of α, β, and δ have been adjusted to account for the energy derived from the chromium removal rate. In this study, the energy derived from the chromium removal rate has been incorporated into our previous findings.[52] The significance of Eqs. [24] through [26] extends beyond visual representation, playing a broader role as they are integrated into streams (α as stream 13, β as stream 14, and δ as stream 20. The volumetric flow rates of oxygen and argon vary over time, as indicated in Table II. Consequently, the fractions of (α, β, and δ) undergo changes. Incorporating kinetic effects is accomplished by adjusting the flow rates in these streams.

$$E_{O_2}^0 = 6.32 \times 10^{-7} \mathrm{Cos}\theta \frac{M_O Q_O^3}{WXn^2 d^3} \qquad [16]$$

$$E_{Ar}^0 = 6.32 \times 10^{-7} \mathrm{Cos}\theta \frac{M_{Ar} Q_{Ar}^3}{WXn^2 d^3}, \qquad [17]$$

where

$$\frac{M_O Q_O^3}{WXn^2 d^3} = \frac{\text{Mass flow rate of oxygen}}{\text{Effective liquid metal}} \qquad [18]$$

Equations [16] and [17] represent liquid metals that are affected by the mass flow rate of oxygen or argon, and this effectiveness (energy transfer) depends on gas flow rates, lance configuration, and geometry of the converter.

6.32×10^{-7}	Constant factor that depends on the geometry of the converter and the nozzle diameter.
$\cos\theta$	The cosine of the angle between the lance and the vertical axis of the converter. This term accounts for the effect of the lance angle on the energy input.
M_O	Molecular weight of oxygen.
M_{Ar}	Molecular weight of argon.
$Q_O:$	Flow rate of oxygen gas, Nm^3/min
$Q_{Ar}:$	Flow rate of argon gas, Nm^3/min
W	Mass of the hot metal (ton).
X	Lance height above the metal bath while blowing (m)
n	Number of nozzles
d	Diameter of each nozzle, m

$$E^0_{decarb} = 6.18 \frac{Q_{decarb} T_{avg}}{W} \left(\ln\left[1 + \frac{\rho g H h_{frac}}{P_{atm}}\right] + \left[1 - \frac{T_0}{T_{avg}}\right] \right) \tag{19}$$

$$E^0_{chromium\,removal} = 6.18 \frac{Q_{chromium\,removal} T_{avg}}{W} \left(\ln\left[1 + \frac{\rho g H h_{frac}}{P_{atm}}\right] + \left[1 - \frac{T_0}{T_{avg}}\right] \right), \tag{20}$$

where

$$Q_{decarb} = \frac{d[C]}{dt} \left(\frac{22.4 \times 60 \times 10^6}{12} \right) \tag{21}$$

$$Q_{chromium\,removal} = \frac{d[Cr]}{dt} \left(\frac{22.4 \times 60 \times 10^6}{52} \right) \tag{22}$$

$\frac{Q_{decarb} T_{avg}}{W}$: Represents the energy required for decarburization per unit weight of hot metal in an AOD steelmaking process

$\frac{Q_{chromium\,removal} T_{avg}}{W}$: Represents the energy required for chromium removal per unit weight of molten metal in an AOD steelmaking process.

$\frac{d[C]}{dt}$: Rate of change of the carbon concentration in the steel bath, tons/min

$\frac{d[Cr]}{dt}$: Rate of change of the chromium concentration in the steel bath, tons/min.

$\ln\left[1 + \frac{\rho g H h_{frac}}{P_{atm}}\right]$: Represents the natural logarithm of the ratio of the partial pressure of oxygen in the gas phase to the atmospheric pressure. This term reflects the influence of the CO flow rate or chromium oxide droplets formation rate on the mass transfer inside the converter.

Equations [19] and [20] denote energy transfer due to carbon or chromium removal influenced by the carbon or chromium removal rates, temperature variations, and inside pressure and dimension of the converter.

H	Height of metal bath, m; g: gravity, m/s^2;
ρ	Density of hot metal, kg/m^3;
h_{frac}	Fraction of height at which CO or chromium oxide droplets form, m
P_{atm}	Atmospheric pressure (bar)
T_0	Initial hot metal temperature (°C)
T_{avg}	Average steel temperature (°C)

$$E^0_{O_2} + E^0_{Ar} + E^0_{decarb} + E^0_{chromium\,removal} = \text{total input energy} = E^0_{total} \tag{23}$$

$$\alpha = 0.09 \left(\frac{E^O_{total}}{8000} \right)^{0.5} \tag{24}$$

$$\beta = 0.3 \left(\frac{E^O_{total}}{8000} \right)^{0.5} \tag{25}$$

$$\Delta = 0.6 \left(\frac{E^O_{total}}{8000} \right)^{0.5} \tag{26}$$

The constant 8000 plays a crucial role in standardizing the total input energy, ensuring that the resulting fractions denoted as (α, β and δ) remain within a practical range. This normalization is of paramount importance in avoiding fractions that might otherwise become either excessively minuscule or disproportionately large. By doing so, it helps sustain uniformity when assessing computed outcomes against actual observations, thereby aligning the model's predictions with empirical data. The explanation for obtaining the coefficients 0.09, 0.3, and 0.6 is shown in Appendix 1

D. Methods and Materials

Samples of slag, metal, and temperature were collected from five distinct heats just before and after the reduction stage during the AOD blowing process. The average of these samples was taken. Subsequently, standard analytical methods, specifically spectrometry, were applied. The procedures involved cutting, grinding, and polishing to determine the compositions of the collected slag and metal samples, while temperature measurements were also recorded.

The chromium removal rate is calculated as follows:

$\frac{dCr}{dt}$: (wt pct chromium at initial in reactor 1 × total wt of initial hot metal—wt pct chromium in the reactor 1 at ith step × total weight of the hot metal in reactor 1 at ith step).

$\left(\frac{dCr}{dt}\right)_{hotspotzone}$: (wt pct chromium at beginning in reactor 3 × total wt at beginning hot metal in reactor

$3 \times$ alpha(α)—wt pct chromium at ith step in reactor 3 $\times$ total weight of hot metal at ith step in reactor 3). $\left(\dfrac{dCr}{dt}\right)_{emulsionzone}$: (wt pct chromium at the beginning in reactor 4 $\times$ total weight at the beginning hot metal in reactor 4 $\times$ beta (β)—wt pct chromium at ith step in reactor 4 $\times$ total weight of the hot metal at ith step in reactor 4).

Carbon, silicon and manganese removal rates were calculated similar approach to chromium removal rate. Where the time step is denoted by i and $i = 1$ to 40.

E. *Input Data and Model Assumptions*

(1) The study involved the computation of heat losses for different components associated with the flow of heat into and out of the converters, with the aim of maintaining thermal heat balances. The determined heat losses attributed to chemical reactions throughout the process amounted to 44815.2 MJ. In order to attain thermal equilibrium, the model incorporated a heat input of 1120.38 MJ min^{-1}. Details of the heat loss calculation can be found in Appendix 2.
(2) With a total blowing time of 40 minutes and a time step of 1 minute

III. RESULTS

In the present work, a dynamic control model based on the initial input parameters of Table I and the charging sequence of Table II using FactSage$^{\text{TM}}$ and its macro program facility was developed.

A. *Evolution of Overall Transient Metal Composition*

In Figure 3, the transient compositions of carbon (a), silicon (b), manganese (c), and chromium (d) were compared with both predictions and plant trial data. The results showed that the predicted removal of carbon, silicon, manganese, and chromium aligned with the actual plant trial data. During the initial 10 minutes of the blowing process, the chromium removal rate was determined to be 0.00072 tons per minute, as illustrated in Figure 3d. This specific period (1–10 minutes) was characterized by the nearly complete consumption of oxygen for the oxidation of carbon, silicon, and manganese, resulting in a notably low rate of chromium removal. More precisely, nearly all of the silicon oxidized within the first 5 minutes of the blowing process due to favorable thermodynamic conditions. It's worth noting that after 14 minutes of blowing, the weight percentages of carbon and manganese were observed to be 0.15 and 0.14, respectively. At the end of oxidation period (30 minute of blowing) wt pct weight percentage of carbon, silicon, manganese and chromium were observed 0.008, 0.0003, 0.07 and 16.6.

Table I.   Input Feature to Assess the Current Model's Performance

Input Materials	Elements	Weight Percent
Hot metal	Carbon	1.80
142 tons	Manganese	0.95
	Silicon	0.36
	Chromium	19.27
	Nickle	4.7
Scrap	Carbon	2.1
3.1 tons	Manganese	0.33
	Silicon	0.20
	Chromium	49
	Nickle	3
	Iron	45
Dolomite	MgO	37
1.3 tons	CaO	63
	CaO	92
Lime	MgO	5
5.5 tons	SiO$_2$	3
FeSi	Fe	25
4 tons	Si	75
SiMn	Si	30
2.5 tons	Mn	70
Al (0.5 ton)	Al	94
Initial hot metal temperature	1486 $^{\circ}$C	
Blowing time (min)	40	
O$_2$ flow rate (Nm^3/min)	140	

Frequent variations and uncertainties in input material composition and measurement errors, relying on average values from 5 heats ensures the reliability and consistency of the results. This approach is crucial for accurate calculations, particularly in the context of the dynamic operational conditions inherent in Argon Oxygen Decarburization, which vary from heat to heat. Therefore, the utilization of average values from multiple heats with similar input types (Grade 316) is a strategic measure to enhance the robustness of the calculations and maintain the overall reliability and consistency of the obtained results..

B. *Evolution of Overall Transient Steel Composition Rate*

In Figure 4, the comprehensive rates of decarburization, desiliconization, demanganization, and chromium removal, along with their rates within the hot spot zone, emulsion reaction, and metal bath zone, are elucidated over the 1–30 minutes blowing period. Figure 4(a) illustrates the dominance of the decarburization rate in the hot spot zone during the initial 1–12 minutes of blowing. However, subsequent to the 12-minute mark, there is a decline in the decarburization rate within the hot spot zone, accompanied by an escalation in the emulsion zone, progressing towards the end of the decarburization process. Additionally, a discernible contribution to decarburization emanates from the metal bath zone. Figures 4(b), (c) delineate the occurrences of desiliconization and demanganization across both the hot spot and emulsion zones, with a more pronounced presence in the hot spot zone, supplemented by some instances in the metal bath zone. Figure 4(d) highlights that the majority of chromium removal

Table II. Charging Trajectory (HM, Scrap, Flux, Oxygen, and Argon + N₂)

| S. No	Charge Quantity	Charging Rate	Nature
1	142-ton, Hot metal		first, 1 min of blowing (stream 5)
2	3.1-ton, scrap	0.31 ton/min	first 10–20 min of blow at a constant rate (stream 6)
3	6.5-ton, lime	0.54 ton/min	first 1–8 and 30–33 min of blow at a fixed rate (stream 10)
4	1.3-ton, dolomite	0.26 ton/min	first 1–5 min of blowing at a constant rate (stream 11)
5	0.5-ton, Aluminium	0.166 ton/min	30–32 min of blowing at a constant rate (stream 12)
6	4-ton, FeSi	0.8 ton/min	30–34 min of blowing at a constant rate (stream 7)
7	2.5-ton, SiMn	0.5 ton/min	30–34 min of blowing at a constant rate (stream 8)
8	oxygen	140, 32 and 5 Nm³/min	first 1–14, 15–25, and 26–30 minutes at a constant rate, 140, 32, and 5 Nm³/min (stream 15)
9	argon + N₂ (1: 0.5)	46,16,10, and 20 Nm³/min	first 1–14, 15–25, 26–30 and 31–40 minutes at a constant rate, 46 16, 10, and 20 Nm³/min (stream 16)
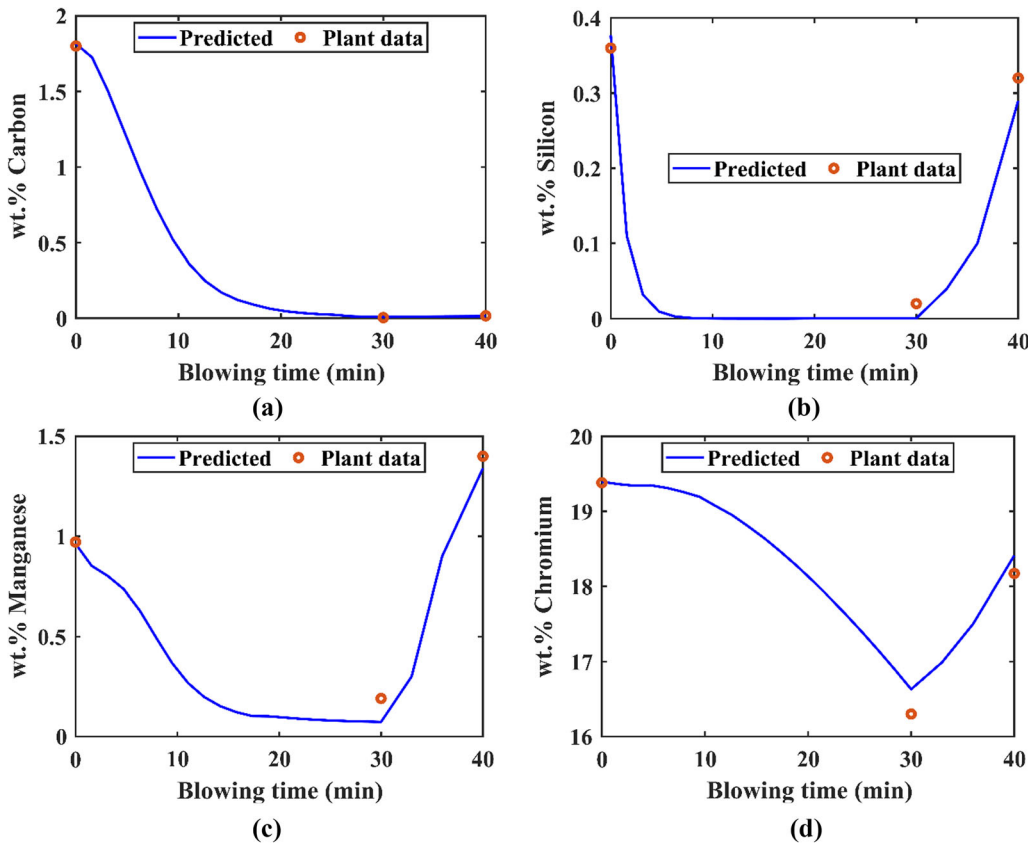
Fig. 3—Comparison of variations wt pct carbon (*a*), silicon (*b*), manganese (*c*), and chromium (*d*), with plant data as a function of blowing times, respectively.

predominantly transpires within the hot spot zone, with only a marginal fraction occurring in both the emulsion and metal bath zones.

In Figure 4, it is examined the simultaneous decarburization, desiliconization, demanganization, and chromium removal processes within the hotspot and emulsion zones and metal bath reactor. The process was segmented into distinct time steps, and it was meticulously assessed the removal rates of various impurities, including carbon [C], silicon [Si], manganese [Mn], and phosphorus [Cr]. These removal rates were found to be intricately dependent on specific conditions, such as temperature, concentration, and slag viscosity.

In our investigation, calculations performed at each time step, considering the dynamic nature of these variable parameters. So, the simulation results are available only after the time step value interval. Consequently, we observed that when the removal rate of
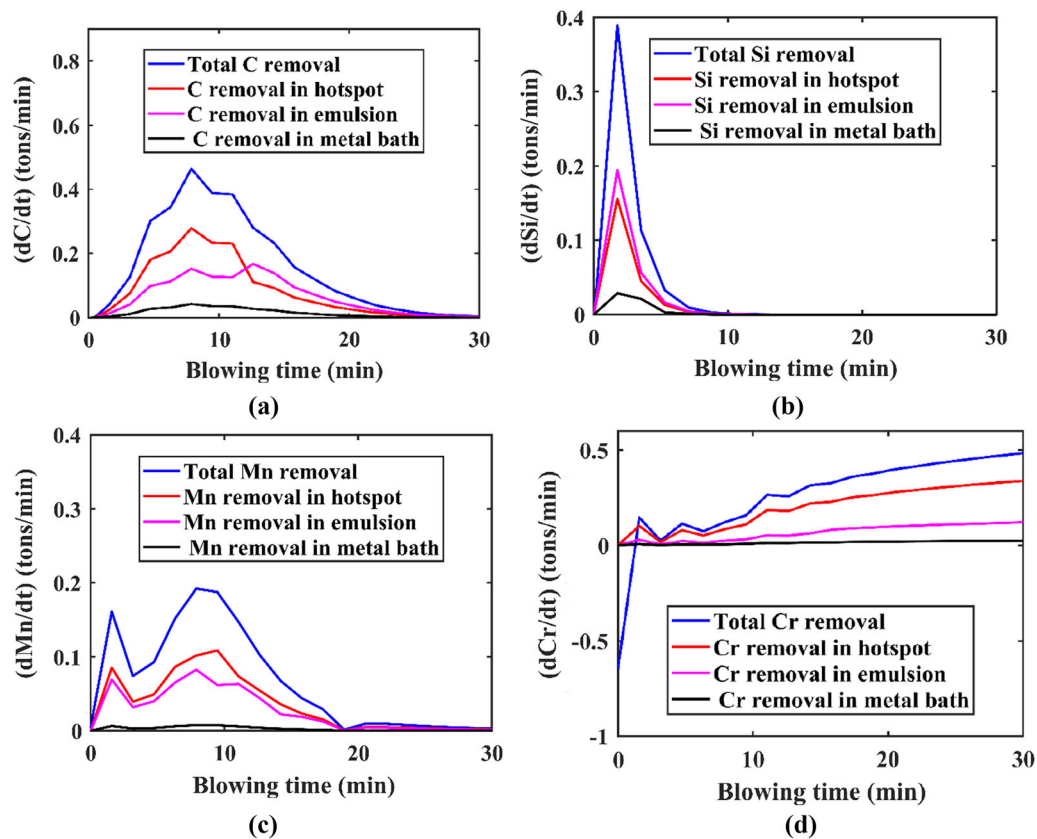
Fig. 4—(a) Comparison of overall decarburization as well as decarburization in hotspot, emulsion reaction and metal bath zones, (b) comparison of overall desiliconization as well as desiliconization in hot spot, emulsion reaction and metal bath zones, (c) comparison of overall demanganization as well as demanganization in hotspot, emulsion reaction and metal bath zones, and (d) comparison of overall chromium removal as well as chromium removal in hot spot, emulsion reaction and metal bath zones as a function of blowing time, respectively (Color figure online).

impurities in one step increased, the subsequent step exhibited increasing or decreasing fluctuations in response to the evolving conditions. This resulted in a complex and dynamic pattern resembling a zigzag trajectory in the impurity removal process.

At 8 minutes of blowing in Figures 4(a) and (c), the highest peak position represents the maximum removal rates achieved at that time. In Figure 4(b), at 2 minutes, the maximum silicon removal rate is achieved.

C. Evolution of Overall Transient Slag Composition

Figure 5 displays the weight percentage (wt pct) distribution of slag compositions for various constituents, with SiO_2, CaO, Cr_2O_3 (a), FeO, MgO and MnO (b). It was found model predicted slag composition were agreed with plant trials. In the initial 5 minutes of the blowing process, the recorded SiO_2 content stands at 19.5 pct, undergoing a subsequent decrease during the 6–30 minutes of blowing and further increases during reduction period (30–40 minutes) Meanwhile, within the first 1–12 minutes, there is a significant reduction in FeO concentration from an initial 11.5 to 4.43 pct, aligning with the refining process for carbon (C), silicon (Si), manganese (Mn), and chromium (Cr). Over the 1–13-minutes period, the CaO concentration in

the slag experiences an increase, likely attributed to the addition of lime during this time. Notably, in the first 1–6 minutes of blowing, the wt pct of Cr_2O_3 in the slag remains relatively low at 6 pct. However, post this period, there is a steady increase, ultimately reaching 39.5 wt pct. Cr_2O_3 concentration significantly decreases from 39.5 to 2.1 pct due to additions of ferroalloy and aluminium.

D. Temperature Trajectory

Figure 6 presents a visual depiction of temperature fluctuations within the system, highlighting crucial variables: the metal bath temperature, the temperature in the slag bath, hotspot and the emulsion zones. Predicted steel temperature is good agree with actual temperature. Specifically, the metal bath temperature exhibited a substantial range from 1487 °C to 1745 °C. Concurrently, the temperature within the slag bath zone displayed variability, spanning from 1467°°C to 1766°C. Notably, the hotspot zone temperature demonstrated fluctuations ranging between 1872 °C and 2750 °C and emulsion zone temperature varies from 1532°°C to 1790°°C. It was found that different between metal bath, slag bath and emulsion zones temperatures vary from 40°°C to 60°°C. The significant temperature contrast
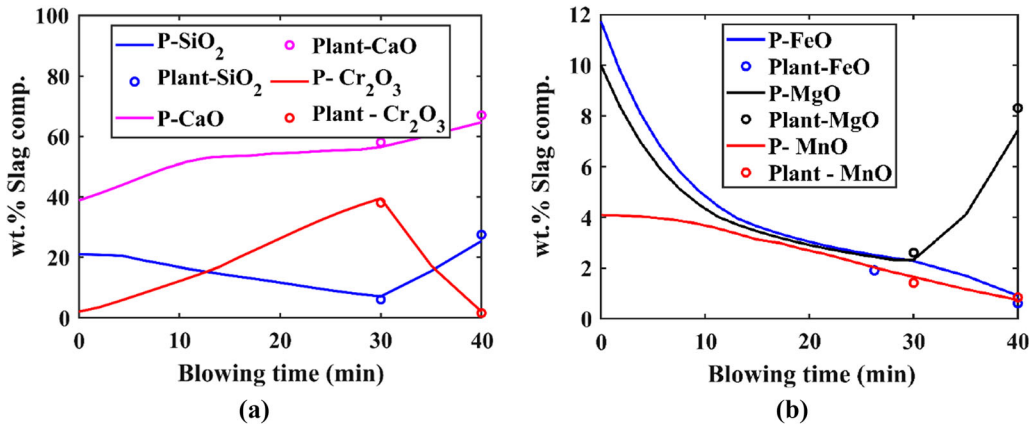
Fig. 5—Slag composition variation (wt pct) of (*a*) SiO₂, CaO, Cr₂O₃, (*b*) FeO, MgO and MnO with plant data as a function of blowing time (Color figure online).
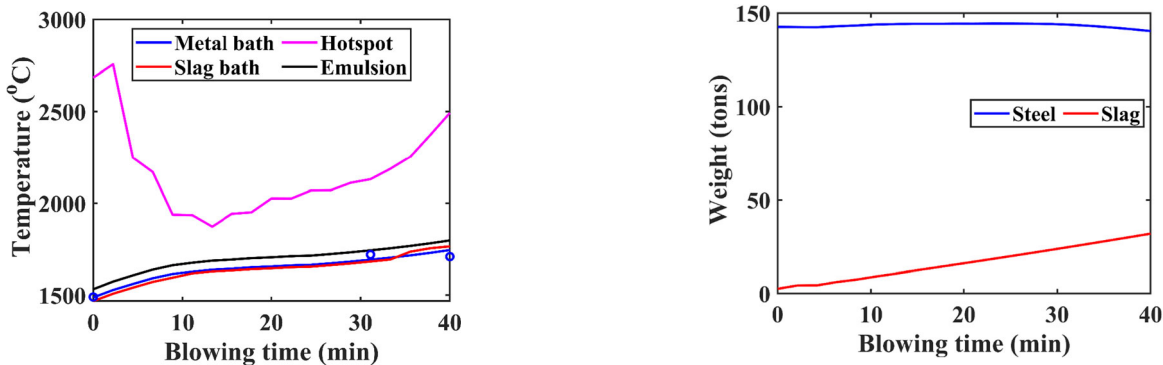

Fig. 6—Temperature variations of liquid stainless -steel or reactor 1 (blue), slag or reactor 2 (red), hotspot zones or reactor 3 (magenta), emulsion zone, or reactor 4 (black), and actual bath as a function of blowing time (Color figure online).

Fig. 7—Variation of liquid steel (blue) and slag (red) weight with blowing time (Color figure online).

between the metal bath and the hot spot zone arises from the exothermic reactions involving carbon and the oxidation of chromium.

E. *Slag and Steel Weight*

Figure 7 shows a representation of the liquid steel and slag weights as a function of blowing time. In the stage of blowing, spanning 1 to 30 minutes, there is a gradual rise in the weight of the slag. Contrastingly, in the concluding blowing phase, from 31 to 40 minutes the increase in slag weight becomes more distinct. This phenomenon can be linked to the addition of ferroalloy and lime as depicted in Figure 5.

IV. DISCUSSION

At each time step, the values of alpha (α) and beta (β) represent the fractions of metal going to reactors 3 (hotspot zone) and 4 (emulsion zone), respectively. alpha (α) and beta (β) are crucial indicators of the gas-metal and metal-slag system mixing and mass transfer processes. These alphas (α) and beta (β) greatly

depend on oxygen and argon flow rates. Fluctuations in the oxygen-to-argon ratio impact these indicators throughout the duration. A fundamental aspect of the execution is dividing the process into various time steps. During the decarburization stage (1–30 minutes), the melt undergoes a reduction in carbon content by introducing a mixture of oxygen and (argon + nitrogen) gases. Alongside carbon, elements like Si, Mn, and Cr, dissolved in the melt, undergo oxidation. To mitigate the oxidation of chromium, the oxidation rate is reduced by adjusting the oxygen-to-argon gas ratio, thereby decreasing the partial pressure of CO. During the initial 1–5 minutes of the blowing phase, favorable thermodynamic conditions result in notably high rates of silicon removal, mimicking practical converter operations. Lime and dolomitic lime are typically introduced just before the oxygen blowing to flux the transfer slag and facilitate the removal of silicon from the metal. Silicon undergoes oxidation before carbon during the oxygen-blowing process. The chemical reactions occurred among metal droplets, slag, and rising gases - specifically at the metal–gas, metal–slag, and slag–gas interfaces within reactors 3 and 4. Additionally, there was a refining contribution from the metal bulk bath (reactor 1) due to the dissolved oxygen in the bath. In the initial 1–10 minutes of blowing, decarburization prevails in the

hotspot zone over the emulsion zone, primarily because of a higher mass flow rate (α). The increase in alphas (α) is attributed to a higher oxygen flow rate. Beyond the first 10 minutes of blowing, there is an increase in Cr_2O_3 content, aiding in carbon oxidation. Consequently, decarburization becomes dominant in the emulsion zone. Just before the oxygen blowing, iron ore is introduced to facilitate the formation of FeO. During the first 1–5 minutes of blowing, desiliconization becomes dominant in the emulsion zone due to the presence of 7 pct FeO and thermodynamic favour conditions. The combination of elevated temperatures and vigorous mixing in the hotspot zone, while the emulsion zone have lower temperatures than the hotspot zone, it is still a region of controlled reactions where metal and slag are intimately mixed. This mixing creates conditions conducive to the oxidation of manganese, along with the controlled reaction environment contributes to the occurrence of manganese oxidation in both zones during the AOD process. The dominance of chromium oxidation in the hotspot zone, over the emulsion zone, can be attributed to the elevated temperatures and vigorous mixing present in the hotspot zone. In this zone, the heightened temperatures significantly enhance the kinetics of oxidation reactions, creating conditions conducive to increased chromium oxidation. The increased reactivity observed at higher temperatures favors the formation of chromium oxides in the hotspot zone.

V. CONCLUSIONS

We draw the following conclusions from this study

(1) Model predictions of metal, slag composition, and metal bath temperature before and after reduction period are similar to plant data. It was found that different between metal bath, slag bath and emulsion zones temperatures vary from 40 °C to 60 °C. The significant temperature contrast between the metal bath (1487 °C to 1745 °C) and the hot spot (1872 °C and 2750 °C) zone arises from the exothermic reactions involving carbon and the oxidation of chromium.

(2) In the initial 1 through 6 minutes of blowing, the slag exhibits a relatively low wt pct of Cr_2O_3 at 6 pct. Following this period, there is a consistent upward trend, reaching a peak of 39.5 wt pct Cr_2O_3. However, after this peak, the concentration of Cr_2O_3 experiences a substantial decrease during reduction period from 39.5 pct to 2.1 pct, attributed to the introduction of ferroalloy and aluminium additions.

(3) During the initial 10 minutes of the blowing process, the chromium removal rate was determined to be 0.00072 tons per minute. This specific period was characterized by the nearly complete consumption of oxygen for the oxidation of carbon, silicon, and manganese, resulting in a notably low rate of chromium removal.

(4) Within the initial 1 through 12 minutes, a notable decrease in FeO concentration is observed, dropping from an initial 11.5 pct to 4.43 pct, consistent with the refining of carbon (C), silicon (Si), manganese (Mn), and chromium (Cr). Throughout the 1 through 13 minutes interval, there is a noticeable rise in the CaO concentration in the slag, likely attributable to the introduction of lime during this timeframe

(5) Both the hotspot and emulsion zones contribute to the removal of carbon, silicon, and manganese. However, the removal of chromium is primarily concentrated in the hotspot zone, driven by the favorable thermodynamic conditions prevailing in that region.

CONFLICT OF INTEREST

On behalf of all authors, the corresponding author states that there is no conflict of interest.

APPENDIX 1

Initial, A = B = C = 1

$$\alpha = A\left(\frac{E^O_{total}}{8000}\right)^{0.5} \quad [A1]$$

$$\beta = B\left(\frac{E^O_{total}}{8000}\right)^{0.5} \quad [A2]$$

$$\delta = C\left(\frac{E^O_{total}}{8000}\right)^{0.5} \quad [A3]$$

Now model was run according to Figure 2, corresponding to the input parameters outlined in Table I.

The convergence criteria obtained from plant trials are applied both before and at the end of the reduction stage of the process

Now, to meet converge criteria A, B, and C values changes

Best fitted with plant data when $A = 0.09$, $B = 0.3$, and $C = 0.6$ only. I.e., we finally got the Eqs. [24] through [26]

APPENDIX 2

HEAT LOSS MODEL

The heat of dissolution of C, Si, Mn, Cr, and Ni is 2.11, − 4.67, 0, 0.40, and 0 KJ/kg

The specific heat of Fe, C, Si, Mn, and Cr is 0.945, 2.278, 3.064, 1.258, and 1.687 KJ/kg

The heat of the formation (1600 °C) of SiO_2, MnO, Cr_2O_3 and FeO are 37.5, 7.1, 11.6 and 6.05 MJ/kg

The sensible heat of steel, CO, CO_2, and slag is 1.413, 1.86. 1.86 and 2.915 MJ/kg

Heat of formation of CaO–SiO_2 is 4.5 MJ/kg of Si

$$
\begin{aligned}
\text{Heat input} =\ & \text{Sensible heat of hot metal} + \text{heat of reaction} \\
=\ & \text{enthalpy of hot metal} + \text{decarburization} \\
& + \text{heat of combustion of CO gas to } CO_2 \\
& + \text{oxidation of silicon, manganese, and} \\
& \quad \text{chromium} + \text{formation of FeO} \\
& + \text{formation of } CaO.SiO_2
\end{aligned}
$$

[A4]

$$
\begin{aligned}
\text{Heat output} =\ & \text{enthalpy of steel} + \text{enthalpy of CO gas} \\
& + \text{enthalpy of } CO_2 \text{ gas} + \text{enthalpy of slag}
\end{aligned}
$$

[A5]

By solving the above two Eqs. [A4] and [A5], we get heat input = 2207.3 MJ and heat output = 1891.7 MJ.

Therefore, heat losses = 315.6 MJ/THM

Total heat losses of the system = 142 × 227.89 = 44815.2 MJ

Heat loss per time step of process = 1120.38 MJ

REFERENCES

1. https://www.worldstainless.org. Accessed 17 June 2023.
2. M. Ersson and A. Tilliander: *Steel Res. Int.*, 2018, vol. 89, p. 1700108.
3. S. Chanouian, B. Ahlin, A. Tilliander, and M. Ersson: *Steel Res. Int.*, 2022, vol. 93, pp. 1–11.
4. T. Ohno and T. Nishida: *Tetsu-to Hagane*, 1977, vol. 63, pp. 2094–99.
5. S. Asai and J. Szekely: *Metall. Trans*, 1974, vol. 5, pp. 651–57.
6. J. Szekely and S. Asai: *Metall. Trans*, 1974, vol. 5, pp. 1573–80.
7. V.V. Visuri, M. Jarvinen, P. Sulasalmi, E.P. Heikkinen, J. Savolainen, and T. Fabritius: *ISIJ Int.*, 2013, vol. 53, pp. 603–12.
8. V.V. Visuri, M. Jarvinen, P. Sulasalmi, E.P. Heikkinen, J. Savolainen, and T. Fabritius: *ISIJ Int.*, 2013, vol. 53, pp. 613–21.
9. V.V Visuri, R Mattila, P Kupari, T.A Fabritius, Comparative study on refractory wear associated with fluxes for AOD slags. In Proceedings of the 7th International Congress on Science and Technology of Steelmaking, Venice 13–15 June 2018.
10. Y. Kang, Y.H. Kim, and H.-S. Sohn: *Met. Mater. Int.*, 2015, vol. 21, pp. 118–25.
11. K. Ashok, P. Sankar, and K. Maruthupandian: *J. Metall. Mater. Sci.*, 2017, vol. 59, pp. 173–80.
12. R. Fruehan: *Ironmak. Steelmak.*, 1976, vol. 3, pp. 153–58.
13. K. Miyamoto, K. Kato, and T. Yuki: *Tetsu -to- Hagane*, 2002, vol. 88, pp. 838–44.
14. S. Yokoyama, M. Takeda, K. Ito, and M. Kawakami: *Tetsu-to Hagane*, 1992, vol. 78, pp. 223–30.
15. T. Nakasuga, K. Nakashima, and K. Mori: *ISIJ Int.*, 2004, vol. 44, pp. 665–72.
16. T. Nakasuga, H. Sun, K. Nakashima, and K. Mori: *ISIJ Int.*, 2001, vol. 41, pp. 937–44.
17. T. Nakasuga, H. Sun, K. Nakashima and K. Mori: Proceeding of the 2nd International Conference on processing materials for properties, vol. 86, TMS, Warrendale, PA, 2000, pp. 553.
18. E. Shibata, S. Egawa, and T. Nakamura: *ISIJ Int.*, 2002, vol. 42, pp. 609–13.
19. K. Taoka, M. Tada, H. Nomura, and H. Baba: *Tetsu-to-Hagane*, 1990, vol. 76, pp. 1863–870.
20. M. Jarvinen, S. Pisila, A. Karna, T. Fabritius, T. Ikaheimonen, and P. Kupari: *Steel Res. Int.*, 2011, vol. 82, pp. 638–49.
21. M. Jarvinen, S. Pisila, A. Karna, T. Fabritius, T. Ikaheimonen, and P. Kupari: *Steel Res. Int.*, 2011, vol. 82, pp. 650–57.
22. J.-H. Wei and D.-P. Zhu: *Metall. Mater. Trans. B*, 2002, vol. 33, pp. 111–19.
23. J.H. Wei and D.P. Zhu: *Metall. Mater. Trans. B*, 2002, vol. 33, pp. 121–27.
24. M. Gornerup and P. Sjoberg: *Ironmak. Steelmak.*, 1999, vol. 26, pp. 58–63.
25. Wei Chi-ho and A. Mitchell, Application of mathematical and physical models in the iron and steel industry, In Proceeding 3rd Process Technology Conference, March 28–31, 1982, ISS, Pittsburgh, PA, vol. 3, pp. 232–254.
26. A. Mitchell, F.R. Carmona, and C. Wei: *Iron Steelmak*, 1982, vol. 3, pp. 37–41.
27. J. Wei and A. Mitchell: *Chin. J. Met. Sci. Technol.*, 1986, vol. 2, pp. 11–23.
28. J. Wei and A. Mitchell: *Acta Metall. Sin.*, 1989, vol. 23, pp. 126–34.
29. W. Jihe: *Chin. J. Met. Sci. Technol.*, 1989, vol. 5, pp. 32–46.
30. E. Shibata, H. Sun, and K. Mori: *Metall. Mater. Trans. B*, 1999, vol. 30, pp. 279–86.
31. M. Gornerup and A.K. Lahiri: *Ironmak. Steelmak.*, 1998, vol. 25, pp. 317–22.
32. B. Deo and S. Kumar: *Adv Mat Res*, 2013, vol. 794, pp. 50–62.
33. J. Riipi, T. Fabritius, E.-P. Heikkinen, P. Kupari, and A. Karna: *ISIJ Int.*, 2009, vol. 49, pp. 1468–476.
34. E.P. Heikkinen, V.V. Visuri and T. Fabritius, Proceeding of the 8th European Oxygen Steelmaking Conference, Associazione Italiana di Metallurgia, Taranto 2018.
35. P. Ternstedt, G. Runnsjo, A. Tilliander, J. Janis, N.A.I. Andersson, and P.G. Jonsson: *Metals*, 2020, vol. 10, p. 308.
36. E.P. Heikkinen, T.M.J. Fabritius, T.M.T. Kokkonen, and J.J. Harkki: *Steel Res. Int.*, 2004, vol. 75, pp. 800–806.
37. P. Ternstedt, R. Gyllenram, J. Bengtsson and P.G. Jonsson, Proceeding of the 4th International Conference on Modelling and Simulation of Metallurgical Processes in Steelmaking, Stahlinstitut VDEh, Düsseldorf 2011.
38. E. Wimmer, D. Kahrimanovic, K. Pastucha, B. Voraberger, and G. Wimmer: *Berg Huettenmaenn Monatsh*, 2020, vol. 165, pp. 3–10.
39. H.J. Odenthal, U. Thiedemann, U. Falkenreck, and J. Schlueter: *Metall. Trans. B*, 2010, vol. 41B, pp. 396–413.
40. C. Wuppermann, N. Giesselmann, A. Ruckert, H. Pfeifer, H.J. Odenthal, and E. Hovestadt: *ISIJ Int.*, 2012, vol. 52, pp. 1817–823.
41. C. Wuppermann, A. Ruckert, H. Pfeifer, and H.J. Odenthal: *ISIJ Int.*, 2013, vol. 53, pp. 441–49.
42. W. Wei, J. Gustavsson, P.B. Samuelsson, R. Gyllenram, A. Tilliander, and P.G. Jonsson: *Ironmak. Steelmak.*, 2022, vol. 49, pp. 70–82.
43. A. Illiander, L.T.I. Jonsson, and P.G. Jonsson: *Steel Res. Int.*, 2014, vol. 85, pp. 376–87.
44. P. Amuelsson, P. Ternstedt, A. Tilliander, A. Appell, and P.G. Jonsson: *Ironmak. Steelmak.*, 2017, vol. 45, pp. 1–7.
45. S. Patra, J. Nayak, L.K. Singhal, and S. Pal: *Steel Res. Int.*, 2017, vol. 88, p. 1600271.
46. P. Ternstedt, P. Ni, N. Lundqvist, A. Tilliander, and P.G. Jonsson: *Ironmak. Steelmak.*, 2018, vol. 45, pp. 944–50.
47. E.P. Heikkinen, V.V Visuri, T. Fabritius, In Proceedings of the 8th European Oxygen Steelmaking Conference, Taranto 10–12 October 2018.
48. A. Rafiei, G.A. Irons, and K.S. Coley: *Metall. Mater. Trans. B*, 2021, vol. 52, pp. 2509–25.

49. P. Mason, A.N. Grundy, R. Rettig, L. Kjellqvist, J. Jeppsson, J. Bratberg, 11th In International Symposium on High-Temperature Metallurgical Processing. The Minerals, Metals & Materials Series. Springer, Cham. 2020.
50. A.N. Grundy, M. Powell, R. Rettig, L. Kjellqvist, J. Jeppsson, A. Jansson, J. Bratberg, A Kinetic and Thermodynamic Description of the Steel Making Process using Thermo-Calc and the CALPHAD Database TCOX. https://thermocalc.com/products/add-on-modules/process-metallurgy-module/. Accessed 1 October 2023.
51. www.factsage.com. Accessed 10 August 2022.
52. P. Singha and A.K. Shukla: *Metals*, 2022, vol. 12, p. 638.